Polarization and cross section of midrapidity J/ψ production in $p+p$ collisions at $\sqrt{s}=510$ GeV

U. Acharya,[20] A. Adare,[11] C. Aidala,[42] N. N. Ajitanand,[60,*] Y. Akiba,[55,56,†] R. Akimoto,[10] M. Alfred,[23] N. Apadula,[28,61] Y. Aramaki,[55] H. Asano,[35,55] E. T. Atomssa,[61] T. C. Awes,[51] B. Azmoun,[7] V. Babintsev,[24] M. Bai,[6] N. S. Bandara,[41] B. Bannier,[61] K. N. Barish,[8] S. Bathe,[5,56] A. Bazilevsky,[7] M. Beaumier,[8] S. Beckman,[11] R. Belmont,[11,42,49] A. Berdnikov,[58] Y. Berdnikov,[58] L. Bichon,[65] D. Black,[8] B. Blankenship,[65] J. S. Bok,[48] V. Borisov,[58] K. Boyle,[56] M. L. Brooks,[38] J. Bryslawskyj,[5,8] H. Buesching,[7] V. Bumazhnov,[24] S. Campbell,[12,28] V. Canoa Roman,[61] C.-H. Chen,[56] C. Y. Chi,[12] M. Chiu,[7] I. J. Choi,[25] J. B. Choi,[30,*] T. Chujo,[64] Z. Citron,[66] M. Connors,[20] M. Csanád,[15] T. Csörgő,[67] A. Datta,[47] M. S. Daugherity,[1] G. David,[7,61] K. DeBlasio,[47] K. Dehmelt,[61] A. Denisov,[24] A. Deshpande,[56,61] E. J. Desmond,[7] L. Ding,[28] A. Dion,[61] J. H. Do,[68] A. Drees,[61] K. A. Drees,[6] J. M. Durham,[38] A. Durum,[24] A. Enokizono,[55,57] H. En'yo,[55] R. Esha,[61] S. Esumi,[64] B. Fadem,[43] W. Fan,[61] N. Feege,[61] D. E. Fields,[47] M. Finger,[9] M. Finger, Jr.,[9] D. Firak,[14] D. Fitzgerald,[42] S. L. Fokin,[34] J. E. Frantz,[50] A. Franz,[7] A. D. Frawley,[19] C. Gal,[61] P. Gallus,[13] P. Garg,[3,61] H. Ge,[61] F. Giordano,[25] A. Glenn,[37] Y. Goto,[55,56] N. Grau,[2] S. V. Greene,[65] M. Grosse Perdekamp,[25] Y. Gu,[60] T. Gunji,[10] H. Guragain,[20] T. Hachiya,[45,55,56] J. S. Haggerty,[7] K. I. Hahn,[17] H. Hamagaki,[10] S. Y. Han,[17,33] J. Hanks,[61] S. Hasegawa,[29] X. He,[20] T. K. Hemmick,[61] J. C. Hill,[28] A. Hodges,[20] R. S. Hollis,[8] K. Homma,[22] B. Hong,[33] T. Hoshino,[22] J. Huang,[7,38] S. Huang,[65] Y. Ikeda,[55] K. Imai,[29] Y. Imazu,[55] M. Inaba,[64] A. Iordanova,[8] D. Isenhower,[1] D. Ivanishchev,[53] B. V. Jacak,[61] S. J. Jeon,[44] M. Jezghani,[20] Z. Ji,[61] J. Jia,[7,60] X. Jiang,[38] B. M. Johnson [7,20] E. Joo,[33] K. S. Joo,[44] D. Jouan,[52] D. S. Jumper,[25] J. H. Kang,[68] J. S. Kang,[21] D. Kawall,[41] A. V. Kazantsev,[34] J. A. Key,[47] V. Khachatryan,[61] A. Khanzadeev,[53] A. Khatiwada,[38] K. Kihara,[64] C. Kim,[33] D. H. Kim,[17] D. J. Kim,[31] E.-J. Kim,[30] H.-J. Kim,[68] M. Kim,[59] Y. K. Kim,[21] D. Kincses,[15] E. Kistenev,[7] J. Klatsky,[19] D. Kleinjan,[8] P. Kline,[61] T. Koblesky,[11] M. Kofarago,[15,67] J. Koster,[56] D. Kotov,[53,58] B. Kurgyis,[15] K. Kurita,[57] M. Kurosawa,[55,56] Y. Kwon,[68] R. Lacey,[60] J. G. Lajoie,[28] D. Larionova,[58] M. Larionova,[58] A. Lebedev,[28] K. B. Lee,[38] S. H. Lee,[28,42,61] M. J. Leitch,[38] M. Leitgab,[25] N. A. Lewis,[42] X. Li,[38] S. H. Lim,[11,54,68] M. X. Liu,[38] S. Lökös,[15] D. Lynch,[7] T. Majoros,[14] Y. I. Makdisi,[6] M. Makek,[66,69] A. Manion,[61] V. I. Manko,[34] E. Mannel,[7] M. McCumber,[38] P. L. McGaughey,[38] D. McGlinchey,[11,38] C. McKinney,[25] A. Meles,[48] M. Mendoza,[8] B. Meredith,[12] W. J. Metzger,[16] Y. Miake,[64] A. C. Mignerey,[40] A. J. Miller,[1] A. Milov,[66] D. K. Mishra,[4] J. T. Mitchell,[7] Iu. Mitrankov,[58] S. Miyasaka,[55,63] S. Mizuno,[55,64] P. Montuenga,[25] T. Moon,[33,68] D. P. Morrison,[7] S. I. Morrow,[65] T. V. Moukhanova,[34] B. Mulilo,[33,55] T. Murakami,[35,55] J. Murata,[55,57] A. Mwai,[60] S. Nagamiya,[32,55] J. L. Nagle,[11] M. I. Nagy,[15] I. Nakagawa,[55,56] H. Nakagomi,[55,64] K. Nakano,[55,63] C. Nattrass,[62] S. Nelson,[18] P. K. Netrakanti,[4] M. Nihashi,[22,55] T. Niida,[64] R. Nouicer,[7,56] N. Novitzky,[31,61,64] A. S. Nyanin,[34] E. O'Brien,[7] C. A. Ogilvie,[28] J. D. Orjuela Koop,[11] J. D. Osborn,[42] A. Oskarsson,[39] K. Ozawa,[32,64] R. Pak,[7] V. Pantuev,[26] V. Papavassiliou,[48] S. Park,[59,61] S. F. Pate,[48] L. Patel,[20] M. Patel,[28] J.-C. Peng,[25] W. Peng,[65] D. V. Perepelitsa,[7,11,12] G. D. N. Perera,[48] D. Yu. Peressounko,[34] C. E. PerezLara,[61] J. Perry,[28] R. Petti,[7,61] C. Pinkenburg,[7] R. Pinson,[1] R. P. Pisani,[7] M. Potekhin,[7] A. Pun,[48,50] M. L. Purschke,[7] P. V. Radzevich,[58] J. Rak,[31] N. Ramasubramanian,[61] I. Ravinovich,[66] K. F. Read,[51,62] D. Reynolds,[60] V. Riabov,[46,53] Y. Riabov,[53,58] D. Richford,[5] T. Rinn,[25,28] N. Riveli,[50] D. Roach,[65] S. D. Rolnick,[8] M. Rosati,[28] Z. Rowan,[5] J. G. Rubin,[42] J. Runchey,[28] N. Saito,[32] T. Sakaguchi,[7] H. Sako,[29] V. Samsonov,[46,53] M. Sarsour,[20] S. Sato,[29] S. Sawada,[32] B. Schaefer,[65] B. K. Schmoll,[62] K. Sedgwick,[8] J. Seele,[56] R. Seidl,[55,56] A. Sen,[28,62] R. Seto,[8] P. Sett,[4] A. Sexton,[40] D. Sharma,[61] I. Shein,[24] T.-A. Shibata,[55,63] K. Shigaki,[22] M. Shimomura,[28,45] P. Shukla,[4] A. Sickles,[7,25] C. L. Silva,[38] D. Silvermyr,[39,51] B. K. Singh,[3] C. P. Singh,[3] V. Singh,[3] M. Slunečka,[9] K. L. Smith,[19] R. A. Soltz,[37] W. E. Sondheim,[38] S. P. Sorensen,[62] I. V. Sourikova,[7] P. W. Stankus,[51] M. Stepanov,[41] S. P. Stoll,[7] T. Sugitate,[22] A. Sukhanov,[7] T. Sumita,[55] J. Sun,[61] X. Sun,[20] Z. Sun,[14] J. Sziklai,[67] A. Takahara,[10] A. Taketani,[55,56] K. Tanida,[29,56,59] M. J. Tannenbaum,[7] S. Tarafdar,[65,66] A. Taranenko,[46,60] A. Timilsina,[28] T. Todoroki,[55,56,64] M. Tomášek,[13] H. Torii,[10] M. Towell,[1] R. Towell,[1] R. S. Towell,[1] I. Tserruya,[66] Y. Ueda,[22] B. Ujvari,[14] H. W. van Hecke,[38] M. Vargyas,[15,67] J. Velkovska,[65] M. Virius,[13] V. Vrba,[13,27] E. Vznuzdaev,[53] X. R. Wang,[48,56] D. Watanabe,[22] Y. Watanabe,[55,56] Y. S. Watanabe,[10,32] F. Wei,[48] S. Whitaker,[28] S. Wolin,[25] C. P. Wong,[20,38] C. L. Woody,[7] Y. Wu,[8] M. Wysocki,[51] B. Xia,[50] Q. Xu,[65] L. Xue,[20] S. Yalcin,[61] Y. L. Yamaguchi,[10,61] A. Yanovich,[24] I. Yoon,[59] I. Younus,[36] I. E. Yushmanov,[34] W. A. Zajc,[12] A. Zelenski,[6] Y. Zhai,[28] S. Zharko,[58] and L. Zou[8]

(PHENIX Collaboration)

[1]*Abilene Christian University, Abilene, Texas 79699, USA*
[2]*Department of Physics, Augustana University, Sioux Falls, South Dakota 57197, USA*
[3]*Department of Physics, Banaras Hindu University, Varanasi 221005, India*
[4]*Bhabha Atomic Research Centre, Bombay 400 085, India*

[5]Baruch College, City University of New York, New York, New York, 10010 USA

[6]Collider-Accelerator Department, Brookhaven National Laboratory, Upton, New York 11973-5000, USA

[7]Physics Department, Brookhaven National Laboratory, Upton, New York 11973-5000, USA

[8]University of California-Riverside, Riverside, California 92521, USA

[9]Charles University, Ovocný trh 5, Praha 1, 116 36, Prague, Czech Republic

[10]Center for Nuclear Study, Graduate School of Science, University of Tokyo,
7-3-1 Hongo, Bunkyo, Tokyo 113-0033, Japan

[11]University of Colorado, Boulder, Colorado 80309, USA

[12]Columbia University, New York, New York 10027
and Nevis Laboratories, Irvington, New York 10533, USA

[13]Czech Technical University, Zikova 4, 166 36 Prague 6, Czech Republic

[14]Debrecen University, H-4010 Debrecen, Egyetem tér 1, Hungary

[15]ELTE, Eötvös Loránd University, H-1117 Budapest, Pázmány P. s. 1/A, Hungary

[16]Eszterházy Károly University, Károly Róbert Campus, H-3200 Gyöngyös, Mátrai út 36, Hungary

[17]Ewha Womans University, Seoul 120-750, Korea

[18]Florida A&M University, Tallahassee, Florida 32307, USA

[19]Florida State University, Tallahassee, Florida 32306, USA

[20]Georgia State University, Atlanta, Georgia 30303, USA

[21]Hanyang University, Seoul 133-792, Korea

[22]Hiroshima University, Kagamiyama, Higashi-Hiroshima 739-8526, Japan

[23]Department of Physics and Astronomy, Howard University, Washington, D.C., 20059, USA

[24]IHEP Protvino, State Research Center of Russian Federation, Institute for High Energy Physics,
Protvino, 142281, Russia

[25]University of Illinois at Urbana-Champaign, Urbana, Illinois 61801, USA

[26]Institute for Nuclear Research of the Russian Academy of Sciences,
prospekt 60-letiya Oktyabrya 7a, Moscow 117312, Russia

[27]Institute of Physics, Academy of Sciences of the Czech Republic,
Na Slovance 2, 182 21 Prague 8, Czech Republic

[28]Iowa State University, Ames, Iowa 50011, USA

[29]Advanced Science Research Center, Japan Atomic Energy Agency,
2-4 Shirakata Shirane, Tokai-mura, Naka-gun, Ibaraki-ken 319-1195, Japan

[30]Jeonbuk National University, Jeonju, 54896, Korea

[31]Helsinki Institute of Physics and University of Jyväskylä, P.O.Box 35, FI-40014 Jyväskylä, Finland

[32]KEK, High Energy Accelerator Research Organization, Tsukuba, Ibaraki 305-0801, Japan

[33]Korea University, Seoul 02841, Korea

[34]National Research Center "Kurchatov Institute", Moscow, 123098 Russia

[35]Kyoto University, Kyoto 606-8502, Japan

[36]Physics Department, Lahore University of Management Sciences, Lahore 54792, Pakistan

[37]Lawrence Livermore National Laboratory, Livermore, California 94550, USA

[38]Los Alamos National Laboratory, Los Alamos, New Mexico 87545, USA

[39]Department of Physics, Lund University, Box 118, SE-221 00 Lund, Sweden

[40]University of Maryland, College Park, Maryland 20742, USA

[41]Department of Physics, University of Massachusetts, Amherst, Massachusetts 01003-9337, USA

[42]Department of Physics, University of Michigan, Ann Arbor, Michigan 48109-1040, USA

[43]Muhlenberg College, Allentown, Pennsylvania 18104-5586, USA

[44]Myongji University, Yongin, Kyonggido 449-728, Korea

[45]Nara Women's University, Kita-uoya Nishi-machi Nara 630-8506, Japan

[46]National Research Nuclear University, MEPhI, Moscow Engineering Physics Institute,
Moscow, 115409, Russia

[47]University of New Mexico, Albuquerque, New Mexico 87131, USA

[48]New Mexico State University, Las Cruces, New Mexico 88003, USA

[49]Physics and Astronomy Department, University of North Carolina at Greensboro,
Greensboro, North Carolina 27412, USA

[50]Department of Physics and Astronomy, Ohio University, Athens, Ohio 45701, USA

[51]Oak Ridge National Laboratory, Oak Ridge, Tennessee 37831, USA

[52]IPN-Orsay, Univ. Paris-Sud, CNRS/IN2P3, Université Paris-Saclay, BP1, F-91406, Orsay, France

[53]PNPI, Petersburg Nuclear Physics Institute, Gatchina, Leningrad region, 188300, Russia

[54]Pusan National University, Pusan 46241, Korea

[55]RIKEN Nishina Center for Accelerator-Based Science, Wako, Saitama 351-0198, Japan

[56]RIKEN BNL Research Center, Brookhaven National Laboratory, Upton, New York 11973-5000, USA

[57]Physics Department, Rikkyo University, 3-34-1 Nishi-Ikebukuro, Toshima, Tokyo 171-8501, Japan

[58]Saint Petersburg State Polytechnic University, St. Petersburg, 195251 Russia

[59]Department of Physics and Astronomy, Seoul National University, Seoul 151-742, Korea

[60]Chemistry Department, Stony Brook University, SUNY, Stony Brook, New York 11794-3400, USA

[61]Department of Physics and Astronomy, Stony Brook University,
SUNY, Stony Brook, New York 11794-3800, USA

[62]University of Tennessee, Knoxville, Tennessee 37996, USA

[63]Department of Physics, Tokyo Institute of Technology, Oh-okayama, Meguro, Tokyo 152-8551, Japan

[64]Tomonaga Center for the History of the Universe, University of Tsukuba, Tsukuba, Ibaraki 305, Japan

[65]Vanderbilt University, Nashville, Tennessee 37235, USA

[66]Weizmann Institute, Rehovot 76100, Israel

[67]Institute for Particle and Nuclear Physics, Wigner Research Centre for Physics,
Hungarian Academy of Sciences (Wigner RCP, RMKI) H-1525 Budapest 114,
P.O. Box 49, Budapest, Hungary

[68]Yonsei University, IPAP, Seoul 120-749, Korea

[69]Department of Physics, Faculty of Science, University of Zagreb,
Bijenička c. 32 HR-10002 Zagreb, Croatia

The PHENIX experiment has measured the spin alignment for inclusive $J/\psi \to e^+e^-$ decays in proton-proton collisions at $\sqrt{s} = 510$ GeV at midrapidity. The angular distributions have been measured in three different polarization frames, and the three decay angular coefficients have been extracted in a full two-dimensional analysis. Previously, PHENIX saw large longitudinal net polarization at forward rapidity at the same collision energy. This analysis at midrapidity, complementary to the previous PHENIX results, sees no sizable polarization in the measured transverse momentum range of $0.0 < p_T < 10.0$ GeV/c. The results are consistent with a previous one-dimensional analysis at midrapidity at $\sqrt{s} = 200$ GeV. The transverse-momentum-dependent cross section for midrapidity J/ψ production has additionally been measured, and after comparison to world data, a simple logarithmic dependence of the cross section on $\sqrt{s}$ was found.

I. INTRODUCTION

Measurements of heavy quark bound states in hadronic collisions provide unique tools for testing QCD. Charmonium, the bound state of a charm and anticharm quark, is produced predominantly via gluon fusion at Relativistic Heavy Ion Collider (RHIC) kinematics. The J/ψ is a colorless neutral meson with spin 1 and decays with considerable branching ratio into lepton pairs ($\approx 6\%$ each for dielectrons and dimuons). Various theoretical models have been developed to describe the J/ψ production cross section and polarization as a function of transverse momentum, but none can describe both simultaneously. All approaches assume a factorization between the production of the heavy-quark pair, $Q\bar{Q}$, and its hadronization into a meson. Different

approaches differ in the treatment of the hadronization. The color-evaporation model that is based on quark-hadron duality and the color-singlet model (CSM) that only allows hadronization without gluon emissions are the most popular earlier approaches; see Refs. [1,2] for recent reviews of theoretical developments and phenomenological work.

One theoretical approach to J/ψ production is within the rigorous framework of nonrelativistic QCD (NRQCD), which is an effective theory that describes the dynamics of heavy quark bound states at nonrelativistic scales ($\nu = v/c \ll 1$) [3–6]. The large heavy-quark mass scale relative to the hadronization scale, $m_Q \gg \Lambda_{\mathrm{QCD}}$, factorizes the J/ψ production process into the quark-antiquark ($Q\bar{Q}$) pair production at short distance and subsequent formation of the heavy quark meson at long-distance. In the former regime, process-dependent short-distance coefficients are calculated perturbatively, and in the latter nonperturbative regime, the behavior is encoded in long-distance matrix elements (LDMEs). The $Q\bar{Q}$ intermediate states are allowed to have quantum numbers different from those of the final-state meson. The leading-order relativistic corrections, for instance, put the $Q\bar{Q}$ either in the color-singlet (CS) state $^3S_1^{[1]}$ or one of the color-octet (CO) states,

---

[*]Deceased.

[†]akiba@rcf.rhic.bnl.gov

$^1S_0^{[8]}$, $^3S_1^{[8]}$, or $^3P_J^{[8]}$ (J = 0, 1, 2). The relative importance of states with different color and angular momentum quantum numbers is estimated by ν-scaling rules [4]. Including CO states is found to be crucial as their leading-power contributions $\approx \mathcal{O}(\frac{1}{p_T})^4$ show up at leading order, in contrast to the CS terms that only appear at next-to-next-to-leading order. The LDMEs can only be determined from experimental data by fitting them via a global analysis. Several groups that performed global analyses [7–10] successfully described world data for transverse momentum (p_T) spectra, while consistent predictions of the spin alignment measurements for quarkonia remain a challenge.

The spin alignment of a positively charged lepton from a J/ψ decay, commonly known as "polarization," has been measured at the Tevatron [11], RHIC [12,13], and the LHC [14–17]. Measuring spin alignment provides additional tests for the theory and understanding dominant quarkonium production mechanisms in different kinematic regimes. The J/ψ polarization is measured by fitting the angular distribution of a positively charged lepton, shown in Eq. (1), to data and extracting decay angular coefficients,

$$\frac{dN}{d\Omega} \approx 1 + \lambda_\theta \cos^2\theta + \lambda_{\theta\phi}\sin^2\theta \cos 2\phi + \lambda_\phi \sin 2\theta \cos \phi,$$

(1)

where the coefficients λ_θ, $\lambda_{\theta\phi}$, and λ_ϕ are determined most commonly in the helicity (HX) frame [18], Collins-Soper (C-S) frame [19], and Gottfried-Jackson (G-J) frame [20] defined in the J/ψ production plane. Invariant variables are constructed using SO(2) symmetry in choosing the z axis in the production plane. Physical interpretation is straightforward only with these invariant quantities, making direct comparison possible between experimental results in different kinematic regimes. Equation (2) shows the two frame-invariant variables defined in Refs. [21,22] to characterize the decay angular distribution,

$$\tilde{\lambda} = \frac{\lambda_\theta + 3\lambda_\phi}{1 - \lambda_\phi}, \qquad F = \frac{1 + \lambda_\theta + 2\lambda_\phi}{3 + \lambda_\theta}.$$

(2)

Recently, general methods have been developed for finding all independent invariants under rotations for particles with various spin quantum numbers [23–25]. There are also new theoretical developments for less inclusive observables that include looking at the polarization of quarkonia produced in jets [26–29].

Previously, a PHENIX J/ψ measurement at $\sqrt{s} = 510$ GeV in $p + p$ at forward rapidity showed largely longitudinal net polarization (negative angular coefficients) [13], while a prior midrapidity PHENIX measurement at $\sqrt{s} = 200$ GeV was consistent with no strong polarization [12]. The present analysis for midrapidity J/ψ production

in $\sqrt{s} = 510$ GeV collisions is complementary to both previous measurements.

II. EXPERIMENTAL SETUP

In 2013, the PHENIX experiment at RHIC collected data from longitudinally polarized $p + p$ collisions at $\sqrt{s} = 510$ GeV. An integrated luminosity of 136 pb^{-1} was used for J/ψ polarization measurements at midrapidity.

The PHENIX detector is described in detail in Ref. [30]. The PHENIX central arms comprise the east and west arms and cover a pseudorapidity range $|\eta| < 0.35$ and an azimuthal coverage of $\Delta\phi = \frac{\pi}{2}$ for each arm. The PHENIX detector elements used in this analysis include the drift chamber (DC), pad chambers (PC), ring-imaging Čerenkov (RICH) detector, and electromagnetic calorimeter (EMCal). Charged particle tracks are reconstructed with the DC and PC tracking system. These detectors also provide the momentum information of the tracks. The data sample used for this analysis is the sum of events triggered with three different energy deposit thresholds applied in the EMCal. Triggers used in this study are described in more detail in Sec. III and in Ref. [31]. The RICH was used for electron identification. Two sets of 64 quartz-crystal radiators attached to photomultipliers at z positions of ± 144 cm and pseudorapidity $3.1 < |\eta| < 3.9$ were used to trigger hard collision events and to evaluate the collision vertex position. These beam-beam-counters (BBCs) and zero-degree calorimeters were used together to evaluate and compare the luminosities seen by PHENIX. In addition, the silicon vertex detector (VTX) was placed in the west arm around the beam pipe at nominal radii of 2.6, 5.1, 11.8, and 16.7 cm with an acceptance of $|\eta| < 1$ and $\Delta\phi = 0.8\pi$. The total material budget expressed as a percentage of a radiation length is 13.42%. As the VTX was not in operation in 2013, this created a large source of electron background from conversions of direct and decay photons.

III. ANALYSIS PROCEDURE

A. Event selection

Events were triggered by a minimum energy in any 2×2-tower group of the EMCal and associated hits in the RICH, in coincidence with the minimum-bias trigger condition. The various EMCal-RICH trigger (ERT) thresholds for energy deposited in the EMCal were 2.2, 3.7, and 4.7 GeV. Detailed description of the PHENIX ERT system can be found in Ref. [12]. Different scale-down factors were used for each threshold; that is, different fractions of triggered events were written to tape. A logical OR of all these triggers was used for polarization measurements, and only the lowest threshold trigger was required for cross section measurements. The J/ψ candidates are triggered by either or both members of the electron-positron pair. The transverse momentum of electrons is determined by the bending of the track in the magnetic field before the DC.

For electron identification, information from both the RICH and the EMCal was used. At least one photomultiplier tube in the RICH, associated with the track, is required to have fired. The energy E deposited in the EMCal was used for electron identification by requiring an expected $(E - p)/p$ ratio within 3 sigma, where the measured uncertainty is parametrized as a function of E/p. The electron identification efficiency is approximately 90%–95%. Hadrons misidentified as electrons and conversion electrons are subtracted statistically as combinatorial background. Due to the presence of nonoperational silicon vertex detector material located very close to the beam pipe, conversion electrons mimic prompt electrons, and thus direct tagging of conversion electrons would have a very limited efficiency; therefore, tagging is not used.

Due to the partial azimuthal coverage on each side of the PHENIX central-arm detector, different arm combinations in the measurements of decay pair products give access to different pair p_T regions. For instance, high-p_T enhancement is achieved in the sample of J/ψ mesons whose decay dielectrons are detected in the same arm due to their small opening angle in the laboratory frame. The dielectrons detected in the east arm offer a relatively clean high-p_T-enhanced J/ψ sample. The pairs within the west arm were not used in this analysis due to excessive background consisting of γ to e^+e^- conversion caused by presence of the VTX that was not operational. The pairs with one lepton in each arm were used to obtain J/ψ mesons with lower p_T. The number of J/ψ events is determined by fitting the invariant mass of lepton pairs in the data and counting within the mass range between 2.8 and 3.3 GeV/c^2. Combinatorial background attributed to decay electrons from hadrons is eliminated statistically before performing the fit using the like-sign method [32] established in PHENIX. To describe the combinatorial background in the data, the ratio of like-sign mass distributions between the data in the same event and the mixed-event data is used in normalizing the like-sign mass distribution in the mixed-event data. Unlike-sign pairs cannot be used for normalization because their mass distributions contain correlated background, as described below. For this reason, the like-sign method is also referred to as the mixed-event method.

The sum of the signal and residual background components, described by a crystal ball function [33] and an exponential function, respectively, is used to further subtract correlated electron background coming from open-heavy-flavor and Drell-Yan decay processes. Invariant mass distributions for dielectrons measured in the same arm and opposite arms are shown in Fig. 1 along with fit results.

B. Efficiency and acceptance corrections

The Monte Carlo (MC) pseudodata were generated to estimate the effects of detector acceptance and efficiency. Events containing a single J/ψ per event were generated
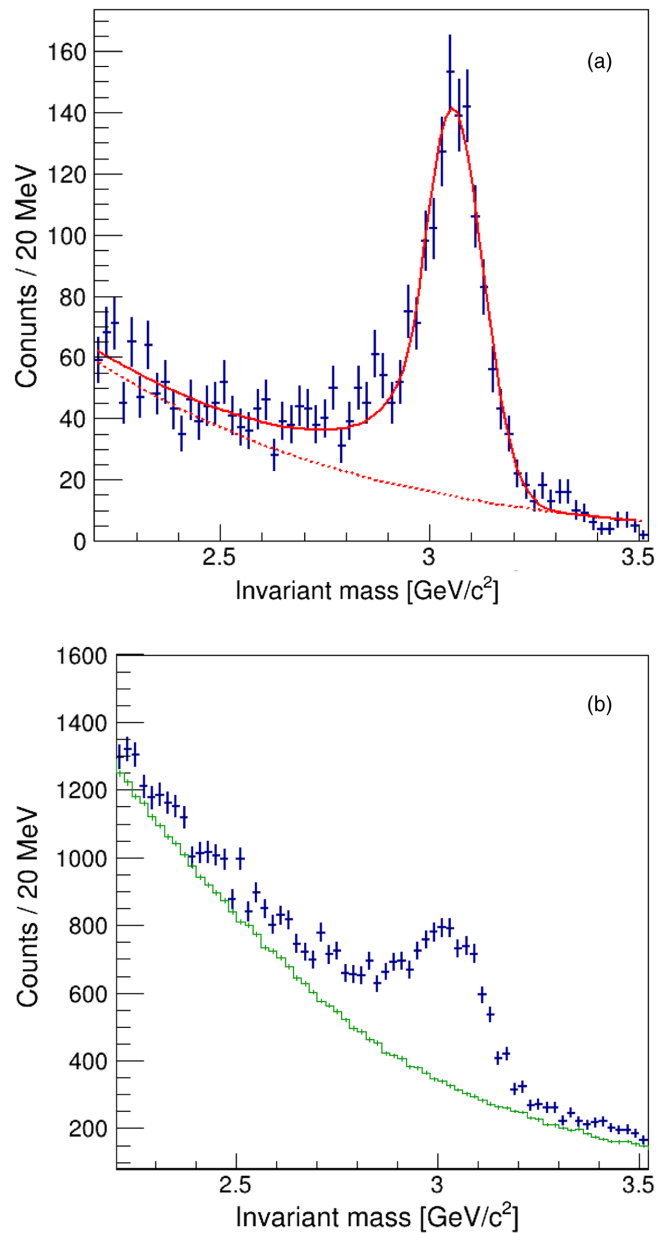

FIG. 1. (a) Example of invariant mass distribution for the high p_T ($3.0 \leq p_T < 10.0$ GeV/c) J/ψ sample. The solid red line indicates a total fit, and the dashed line shows correlated background from the fit. (b) Example of invariant mass distribution for the low-p_T ($0.0 < p_T < 3.0$ GeV/c) sample. Green histogram shows combinatorial background calculated using the mixed-event method and subtracted before fitting.

with zero polarization, a flat p_T distribution, and a flat z-vertex distribution along the beam direction, using MC techniques. The J/ψ's subsequently were forced to decay into dielectrons within the detector acceptance. The yields were then reweighted, as described in more detail below, to emulate effects that are present in the data such as smeared vertex distribution along the beam axis, the shape of the J/ψ p_T distribution, and the ERT trigger efficiencies.
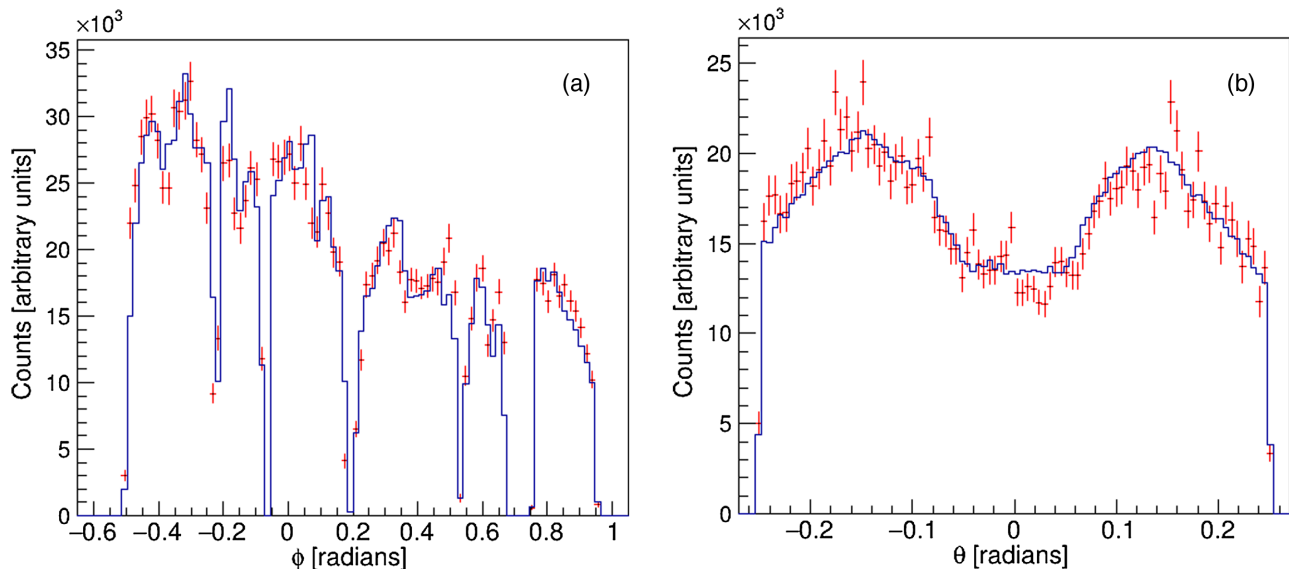
FIG. 2. Comparison of azimuthal angle ϕ (a) and polar angle θ (b) distributions in data (red points) and MC (blue histogram) for electrons.

Polarization measurements are particularly susceptible to inconsistency between the simulation and data as the acceptance corrections accounting for the zero polarization baseline are solely dependent on the simulation. A comparison of the polar and azimuthal angular distributions between the data and MC simulation, after the effects of dead areas, shows good agreement, as seen in Fig. 2.

The shape of $\frac{dN(J/\psi)}{dp_T}$ can affect the polarization extraction in a nontrivial manner due to the limited azimuthal acceptance of the PHENIX central arms. Opposite-sign pairs bending toward each other into the detector populate different phase space than the ones bending away from each other. For this reason, the p_T differential J/ψ cross section has been measured in data. The measured cross section was fit with a Kaplan function, defined in Eq. (3), and the fit results were then used to reweight the MC pseudodata for the acceptance correction,

$$\frac{d\sigma}{dp_T} = \frac{A \cdot p_T}{[1 + (p_T/b)^2]^n}. \tag{3}$$

As the data were sampled from an OR of three triggers with different energy thresholds, a method was developed to emulate the trigger efficiency effect on the p_T shape of the data. The efficiency of triggering on J/ψ events for each type of ERT was determined from the minimum-bias dataset by checking the trigger condition. The acceptance-corrected pseudodata were then processed by randomly sampling the distributions of ERT-measured efficiencies and prescale factors. The detector area masked due to being ineffective or suffering from excessive electron background was taken into account in this method.

The shape of the raw J/ψ yield as a function of p_T in data before corrections is in excellent agreement with the

efficiency corrected normalized yield in simulation for each trigger type as well as for all possible trigger combinations (see Fig. 3).

C. Cross sections

For cross section measurements, the raw J/ψ yield is corrected for trigger efficiencies as well as track reconstruction efficiencies and acceptance. The EMCal
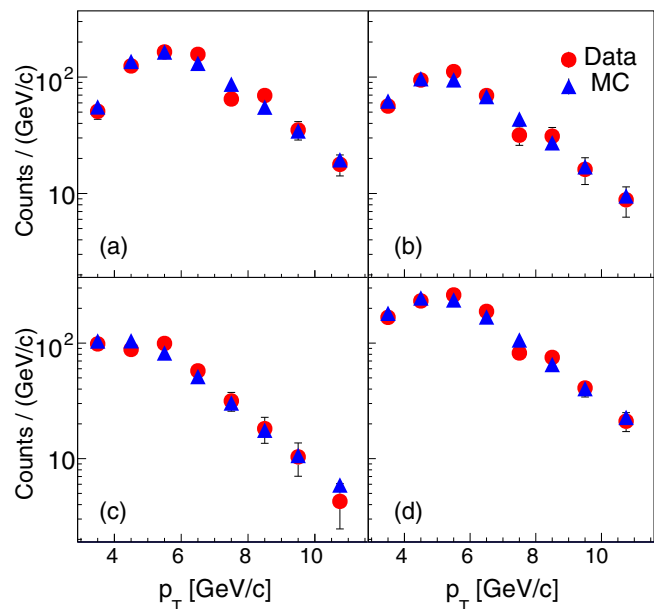

FIG. 3. Comparison of the shapes of J/ψ data and MC vs p_T for events triggered with three different ERT settings [(a) Type A, (b) Type B, (c) Type C] and (d) for all settings inclusive type A + B + C. For direct comparisons, trigger efficiency corrections are applied to MC to describe the data.

trigger efficiencies were measured using data, and the electron reconstruction efficiencies and acceptance corrections were obtained from MC simulation as described in the previous section. An integrated luminosity of 136 pb^{-1} was sampled in the analysis, and the global normalization of the cross section was determined by the $p + p$ cross section sampled by the BBC trigger, which is found to be $32.5 \pm 3.0\,(\text{stat}) \pm 1.2\,(\text{syst})$ mb, based on van der Meer scan results. The effects of multiple collisions per beam crossing due to high luminosity at $\sqrt{s} = 510$ GeV, which were estimated to be of order of 20%, were also taken into account in counting J/ψ yields.

D. Angular coefficients

To account for acceptance and efficiency effects, the raw angular distribution in data is divided by the reweighted single J/ψ MC pseudodata generated under an assumption of no polarization as described in Sec. III B. This procedure closely follows methods described in Ref. [13] and additionally adopts the trigger emulator described in Sec. III B. The $\cos\theta - \phi$ distributions of the decay positron in three different polarization frames in MC pseudodata are shown in Fig. 4.

Angular coefficients were extracted with three different methods; the χ^2 method, the maximum log-likelihood (MLL) method and the parametric bootstrap method [34]. The χ^2 fitting results are displayed in contours at 68.3%, 95.4% and 99.7% confidence level (CL) in Fig. 5. One can see that some of the coefficients are correlated in one frame and uncorrelated in other frames. The HX frame is known to be orthogonal to the C-S frame and similar to the G-J frame at midrapidity, which is also seen in our results. Figure 5 shows that the correlation pattern between λ_θ and λ_ϕ which is represented by the orientation of elliptic fit contours, has better alignment between the HX and G-J frames than with the C-S frame. The MLL method treats low statistics bins more properly than the χ^2 method, while it is prone to underestimating uncertainties as the signal-to-background ratio becomes smaller. In fitting methods, the uncertainties on the invariants that are a function of primary angular coefficients are propagated from the ones on coefficients, taking into account the correlation matrix. The parametric bootstrap method properly estimates uncertainties on the invariant variables. In this method, a Gaussian noise term is added to each measurement point at each sampling trial with a standard deviation of the corresponding measured uncertainty. After a large number of sampling procedures, the uncertainties are defined at a 68% CL.

The results are consistent among different methods within 0.5σ in all frames, and the central measured values and statistical uncertainties from the best-fit results were taken as the final results.

At lower p_T (<3.0 GeV/c), the decay electron and positron are detected in opposite PHENIX central arms.
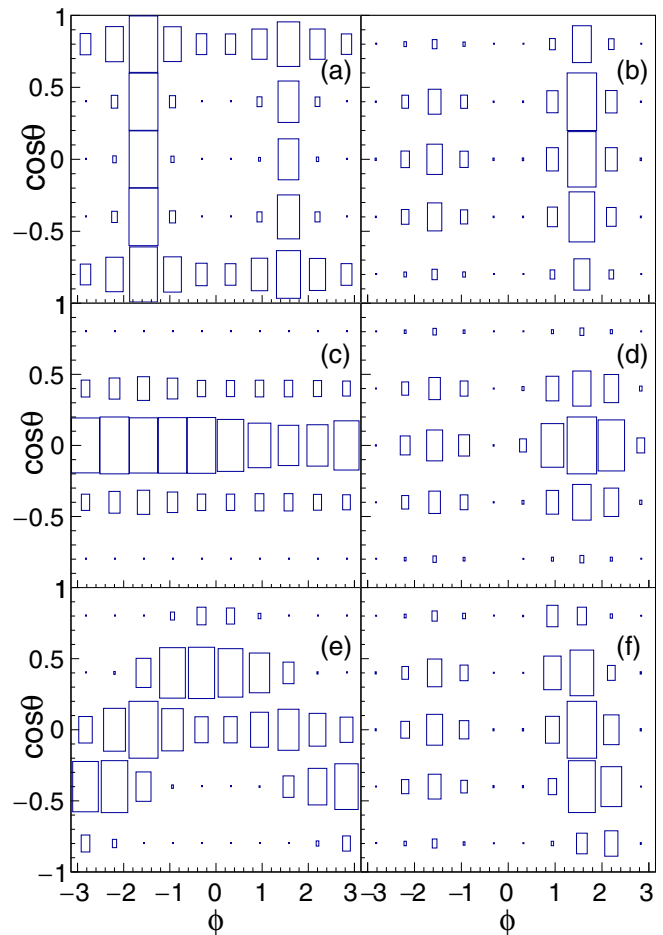

FIG. 4. Polar-azimuthal angular distributions in three different polarization frames [(a) and (b) helicity, (c) and (d) Collins-Soper, (e) and (f) Gottfried-Jackson] for decay positrons in MC pseudodata generated with a flat J/ψ p_T and flat z-vertex distribution. The distributions are reweighted for p_T and z-vertex distribution in the data and corrected for trigger efficiencies. The p_T ranges are (a), (c), and (e) $0.0 < p_T < 3.0$ GeV/c and (b), (d), and (f) $3.0 \leq p_T < 10.0$ GeV/c.

A silicon VTX was installed in the PHENIX west arm but was not operational during the data taking. This resulted in a high level of irreducible electron background originating from photon conversion in the VTX material. These random combinations of background electrons were subtracted using an event mixing technique but resulted in higher statistical and additional systematic uncertainty for the low p_T measurement. The PHENIX acceptance in $\cos\theta - \phi$ space is very different for decay electrons and positrons detected in opposite PHENIX central arms compared to the case when both the electron and positron are detected in the same arm. As a result, the acceptance for the C-S frame turned out to be very limited, and a polarization measurement in this frame was not done at low p_T. The polarization coefficients at low p_T were determined using only the χ^2 fitting method.
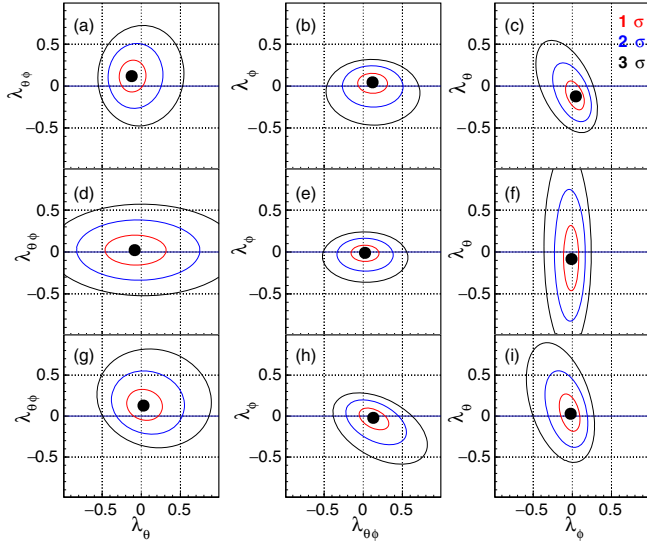
FIG. 5.   The best-fit results for the three angular coefficients are shown with a central value in a dot along with contours at 68.3%, 95.4% and 99.7% confidence levels. The polarization frames are (a), (b), and (c) HX, (d), (e), and (f) C-S, and (g), (h), and (i) G-J. The plot is for the high p_T bin $(3.0 \leq p_T < 10.0 \text{ GcV}/c)$.

E. Systematic uncertainties

Sources of systematic uncertainties on the polarization and cross section measurement include uncertainties on acceptance, tracking and electron identification efficiency, trigger efficiencies, uncertainties on the global normalization derived from the cross section seen by the BBC, and the trigger rate dependence of J/ψ yield counting. The two latter sources do not affect the polarization measurements at all, but they are the main sources of systematic uncertainty for J/ψ cross section determination.

During RHIC run 2013, the proton beam luminosity was very high, which resulted in a non-negligible probability of multiple collisions per beam crossing at high trigger rates. The correction to the J/ψ cross section due to multiple collisions per crossing was calculated by dividing the whole dataset into five run groups with different trigger rates, calculating the cross section for each group, and extrapolating to zero trigger rate. The correction was estimated to be 0.80 ± 0.20. The large uncertainty of this estimate is due to extrapolating from very high trigger rates to zero and lack of statistics. This is the largest systematic uncertainty of the J/ψ cross section.

The primary source of systematic uncertainties on the polarization measurements in the central arm detectors is the shape of the J/ψ p_T spectra. The p_T shape is affected by statistical uncertainties on the raw measured yields as well as uncertainties on the ERT efficiencies. The uncertainties on the ERT efficiencies were estimated using a sampling method. In each sampling trial, parameters were extracted from fitting the efficiency curve for each trigger type, and the analysis was repeated with those parameters to estimate the combined ERT efficiencies. The quadratic sum of the statistical and systematic uncertainties was assigned as a total uncertainty at each measurement point. The systematic uncertainties on angular coefficients that are attributed to p_T shape were estimated using the parametric bootstrap method with a Gaussian noise term corresponding to the aforementioned uncertainties. Uncertainties estimated in this method depend on the p_T of J/ψ, the type of λ coefficient, and the polarization frame. Resulting uncertainties from this source are larger (as high as ≈ 0.5 on λ_θ) at $p_T < 3.0 \text{ GeV}/c$ and < 0.1 in most cases at $p_T \geq 3.0 \text{ GeV}/c$. In addition, the differences between fitting methods, estimated to be less than 0.5 times the statistical uncertainties in all angular coefficients, were added as systematic uncertainties at high p_T.

At low p_T (below $\approx 3.0 \text{ GeV}/c$), the PHENIX acceptance in $\cos\theta - \phi$ space is very different from that at higher p_T. Relative contributions from different sources of systematic uncertainties also change, while the dependence on exact p_T shape remains a dominant factor. An additional systematic uncertainty at low p_T is caused by the much larger combinatorial background, which had to be subtracted using a mixed-event method. This uncertainty was estimated by varying the mixed-event background normalization by $\pm 1\sigma$ and was found smaller than the two uncertainties mentioned above. Systematic uncertainties of this measurement are shown in Table I.

IV. RESULTS

The measured p_T-differential J/ψ cross section is shown in Fig. 6 with a fit to a Kaplan function. Due to the higher

TABLE I.   Results with statistical $\oplus$ total systematic uncertainties.

| Frame	p_T	λ_θ	λ_ϕ	$\lambda_{\theta\phi}$	$\tilde{\lambda}$	F
Helicity	$0.0 < p_T < 3.0$	$0.01^{+(0.44 \oplus 0.24)}_{-(0.24 \oplus 0.31)}$	$0.06^{+(0.20 \oplus 0.23)}_{-(0.35 \oplus 0.27)}$	$0.23^{+(0.12 \oplus 0.09)}_{-(0.08 \oplus 0.11)}$	$0.20^{+(0.32 \oplus 0.48)}_{-(0.35 \oplus 0.52)}$	$0.38^{+(0.06 \oplus 0.06)}_{-(0.09 \oplus 0.10)}$
	$3.0 \leq p_T < 10$	$-0.12^{+(0.18 \oplus 0.04)}_{-(0.16 \oplus 0.06)}$	$0.06^{+(0.11 \oplus 0.07)}_{-(0.13 \oplus 0.07)}$	$0.12^{+(0.19 \oplus 0.04)}_{-(0.19 \oplus 0.04)}$	$0.01^{+(0.30 \oplus 0.20)}_{-(0.37 \oplus 0.19)}$	$0.34^{+(0.07 \oplus 0.04)}_{-(0.08 \oplus 0.05)}$
Collins-Soper	$3.0 \leq p_T < 10$	$-0.08^{+(0.40 \oplus 0.10)}_{-(0.38 \oplus 0.16)}$	$-0.01^{+(0.09 \oplus 0.03)}_{-(0.10 \oplus 0.12)}$	$0.02^{+(0.18 \oplus 0.01)}_{-(0.18 \oplus 0.07)}$	$-0.11^{+(0.47 \oplus 0.22)}_{-(0.47 \oplus 0.17)}$	$0.31^{+(0.11 \oplus 0.05)}_{-(0.11 \oplus 0.05)}$
Gottfried-Jackson	$0.0 < p_T < 3.0$	$0.13^{+(0.52 \oplus 0.35)}_{-(0.59 \oplus 0.52)}$	$0.01^{+(0.06 \oplus 0.07)}_{-(0.05 \oplus 0.10)}$	$-0.01^{+(0.25 \oplus 0.06)}_{-(0.24 \oplus 0.07)}$	$0.17^{+(0.42 \oplus 0.29)}_{-(0.42 \oplus 0.42)}$	$0.37^{+(0.07 \oplus 0.08)}_{-(0.12 \oplus 0.11)}$
	$3.0 \leq p_T < 10$	$0.03^{+(0.24 \oplus 0.13)}_{-(0.21 \oplus 0.05)}$	$-0.02^{+(0.12 \oplus 0.05)}_{-(0.15 \oplus 0.06)}$	$0.13^{+(0.20 \oplus 0.08)}_{-(0.18 \oplus 0.09)}$	$-0.04^{+(0.34 \oplus 0.23)}_{-(0.40 \oplus 0.17)}$	$0.33^{+(0.08 \oplus 0.05)}_{-(0.09 \oplus 0.04)}$
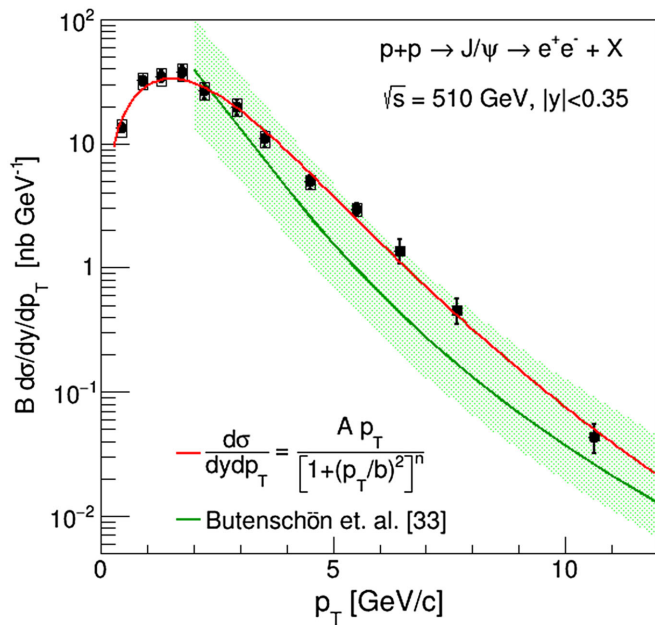
FIG. 6. The measured differential J/ψ cross section times branching ratio as a function of transverse momentum. Fit parameters are $A = 37.6 \pm 2.2$ nb/(GeV/c), $b = 4.33 \pm 0.28$ GeV/c, and $n = 4.61 \pm 0.32$. Open rectangles show systematic point-by-point uncertainties. Global normalization uncertainty of 10.1% is not shown. The green curve shows theory prediction based on full NRQCD at NLO with leading relativistic corrections that include CS and CO states, provided by Butenschön *et al.* [35]. The light green band indicates theory uncertainty.
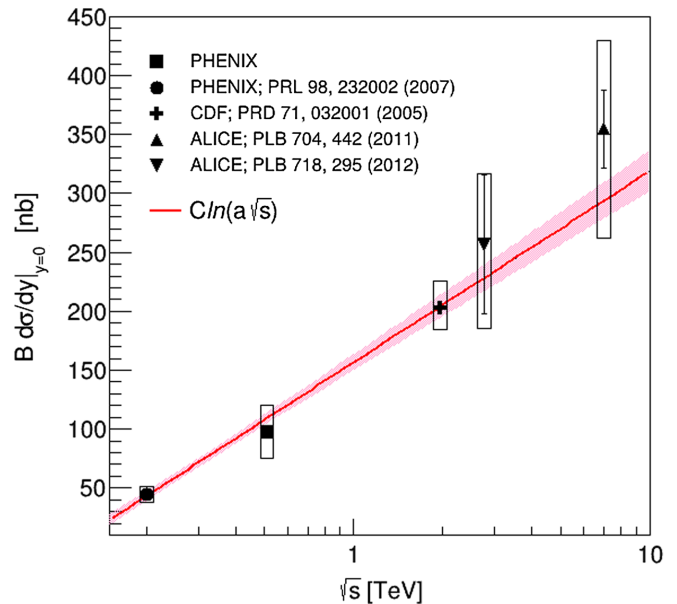

FIG. 7. The PHENIX results of p_T-integrated cross section times branching ratio for J/ψ production at midrapidity, shown with world data. All systematic errors for CDF and ALICE experiments were added in quadrature. The fit parameters are $C = 70.4$ nb, and $a = 9.27$ TeV^{-1}. The pink band shows the one-sigma fit uncertainty.

collision energy, the p_T spectrum is harder than previously published PHENIX results for $\sqrt{s} = 200$ GeV [12], where the fit parameter b that determines the hardness of the spectrum for a given n was estimated to be smaller at 3.41 ± 0.21 and the parameter n was comparable at 4.6 ± 0.4. Figure 6 also shows a comparison of the measured J/ψ differential cross section with a theory prediction based on full NRQCD at next-to-leading-order (NLO) with leading relativistic corrections that includes CS and CO states, provided by Butenschön *et al.* [35]. The sources of theory uncertainties include variations of theory scale and LDMEs. Within its uncertainties, the theory calculation is in agreement with the experimental results within its valid range of $p_T \gtrsim 2$ GeV/c, justifying the use of the theory model for predictions of polarization measurements in this kinematic range.

The p_T-integrated cross section times branching ratio is shown in Fig. 7 along with the previous PHENIX results at $\sqrt{s} = 200$ GeV [36] and the world results from the LHC [37,38] and Tevatron [39]. A simple logarithmic dependence on the collision energy is seen for J/ψ production at midrapidity, making estimates of J/ψ yield at any $\sqrt{s}$ easy and inviting the theory community to model the trend. The p_T-integrated cross section times branching

ratio was found to be $97.6 \pm 3.6\,(\text{stat}) \pm 5.1\,(\text{syst}) \pm 9.8\,(\text{global}) \pm 19.5\,(\text{multiple collision})$ nb.

The final results of the three primary angular coefficients are shown in Figs. 8–10. Uncertainties on measurements in different frames are correlated. Due to limited detector acceptance in η at midrapidity, λ_θ (Fig. 8) is poorly constrained compared to λ_ϕ (Fig. 9). Theory predictions based on full NRQCD at NLO with leading relativistic corrections that includes CS and CO states, provided by Butenschön *et al.* [40], are overlaid with the measurements. The uncertainty bands on the NRQCD predictions account for the scale uncertainties and uncertainties on the LDMEs. The LDMEs were obtained in a global analysis of unpolarized data that excludes measurements from hadroproduction with $p_T < 3.0$ GeV/c. To improve consistency with the data, the feed down from heavier charmonium states was subtracted in the theory prediction. The fraction of J/ψ events from b-flavored hadron decays is negligible at RHIC. In PHENIX, the unpolarized yield measurements [12] are well described down to 1 GeV/c, justifying the comparison to the polarized measurements.

In Figs. 11 and 12, the results are also shown in terms of frame-invariant observables $\tilde{\lambda}$ and F, defined in Eq. (2). Measuring these invariant variables provides a direct test for the underlying production mechanisms. Comparing results in different frames can additionally serve as robust tools to address systematic uncertainties. Consistency between different frames shown for $\tilde{\lambda}$ in Fig. 11 and for F in Fig. 12 indicates that systematic effects are under
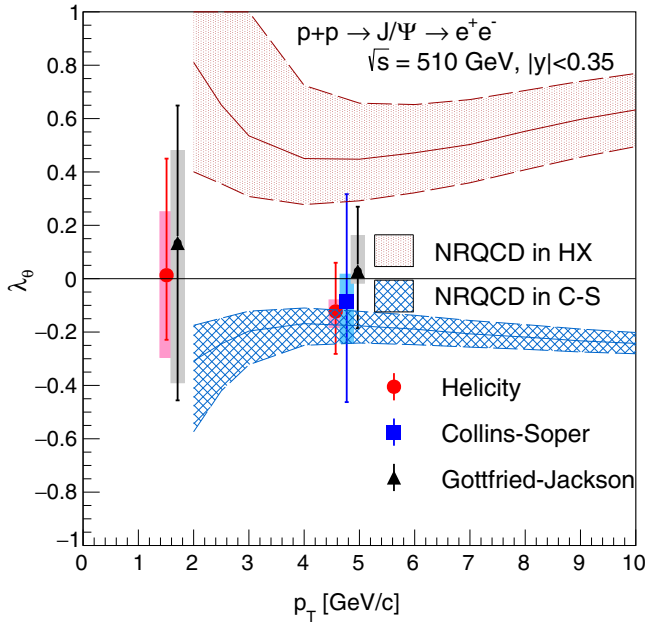
FIG. 8. λ_θ measured in J/ψ transverse momentum bins of $0.0 < p_T < 3.0$ GeV/c and $3.0 \le p_T < 10.0$ GeV/c overlaid with NRQCD predictions in the helicity and Collins-Soper frames. The points for different frames are shifted for visual clarity.
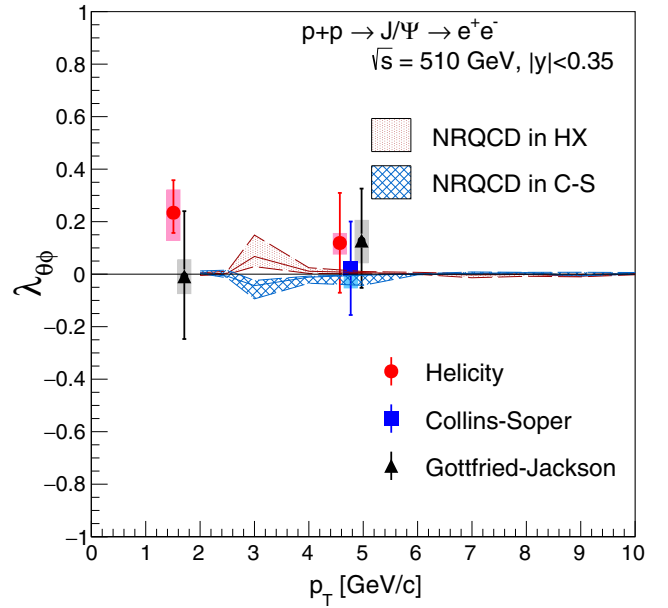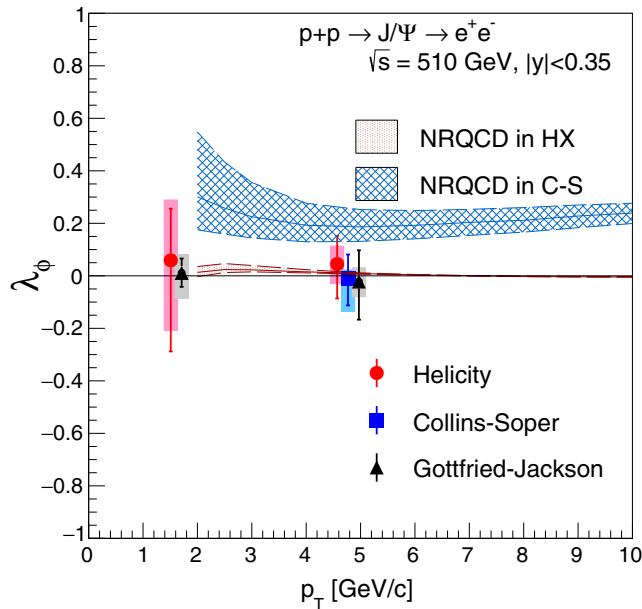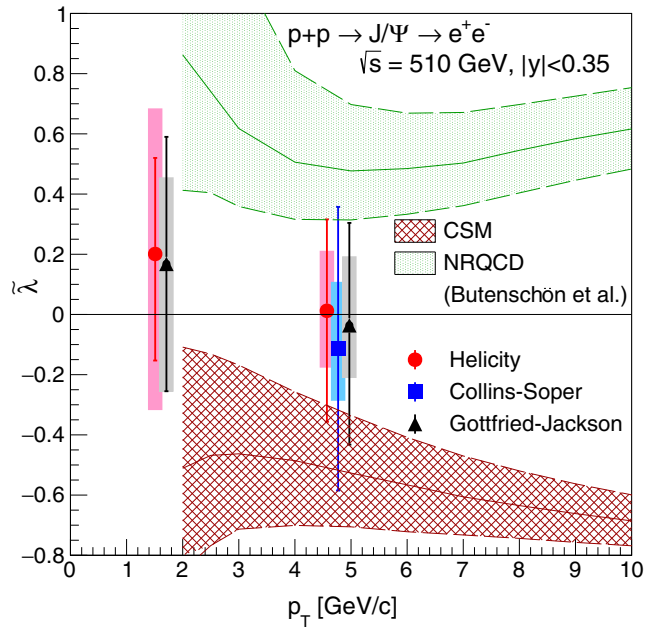

FIG. 10. Angular coefficient $\lambda_{\theta\phi}$ measured in J/ψ transverse momentum bins of $0.0 < p_T < 3.0$ GeV/c and $3.0 \le p_T < 10.0$ GeV/c overlaid with NRQCD predictions in the helicity and Collins-Soper frames. The points for different frames are shifted for visual clarity.

FIG. 9. Angular coefficient λ_ϕ measured in J/ψ transverse momentum bins of $0.0 < p_T < 3.0$ GeV/c and $3.0 \le p_T < 10.0$ GeV/c overlaid with NRQCD predictions in the helicity and Collins-Soper frames. The points for different frames are shifted for visual clarity.

FIG. 11. $\tilde{\lambda}$ measured in J/ψ transverse momentum bins of $0.0 < p_T < 3.0$ GeV/c and $3.0 \le p_T < 10.0$ GeV/c overlaid with CSM and NRQCD predictions in the helicity frame. Predictions for this frame-invariant variable in the other two frames are consistent with the one in the helicity frame. The points for different frames are shifted for visual clarity.
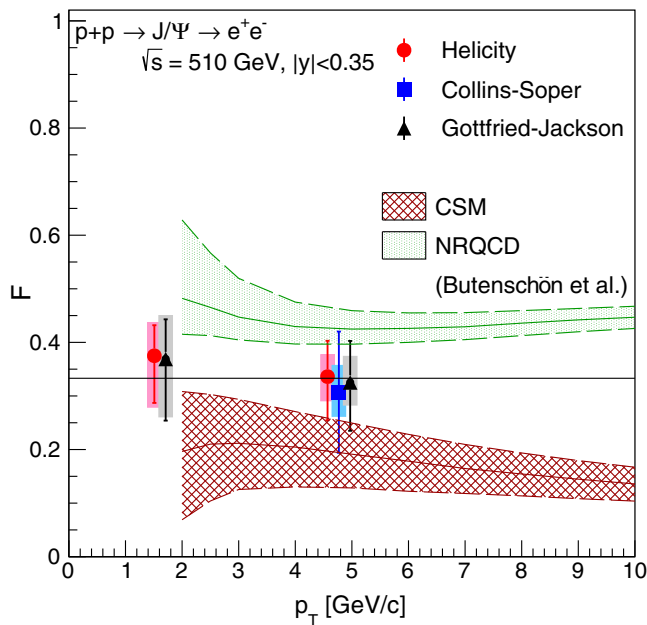
FIG. 12.   Invariant F measured in J/ψ transverse momentum bins of $0.0 < p_T < 3.0$ GeV/c and $3.0 \leq p_T < 10.0$ GeV/c overlaid with CSM and NRQCD predictions in the helicity frame. Predictions for this frame-invariant variable in the other two frames are consistent with the one in the helicity frame. The points for different frames are shifted for visual clarity.

good control. Frame-invariant variables are interpreted as the total net polarization summed over all production mechanisms. Different production mechanisms can lead to natural polarization in different frames. In the case of $\tilde{\lambda}$,
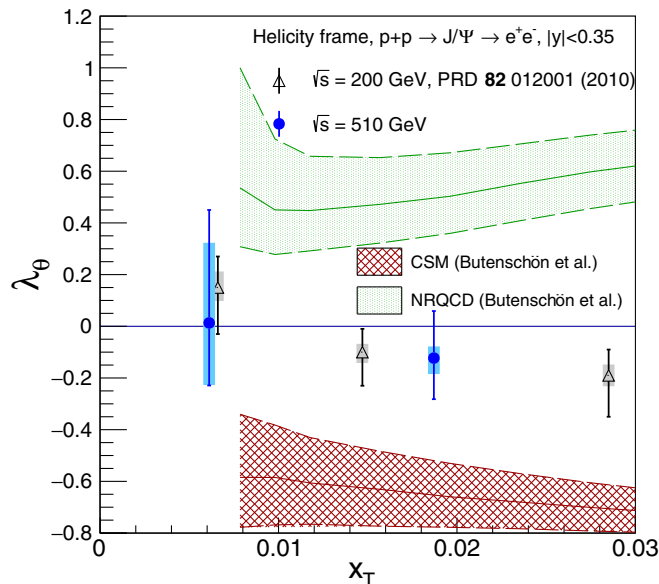
FIG. 13.   Angular coefficient λ_θ of midrapidity J/ψ production at $\sqrt{s} = 200$ and 510 GeV, shown as a function of $x_T = \frac{2p_T}{\sqrt{s}}$. Data points at the lowest p_T have been shifted against each other for visual clarity.
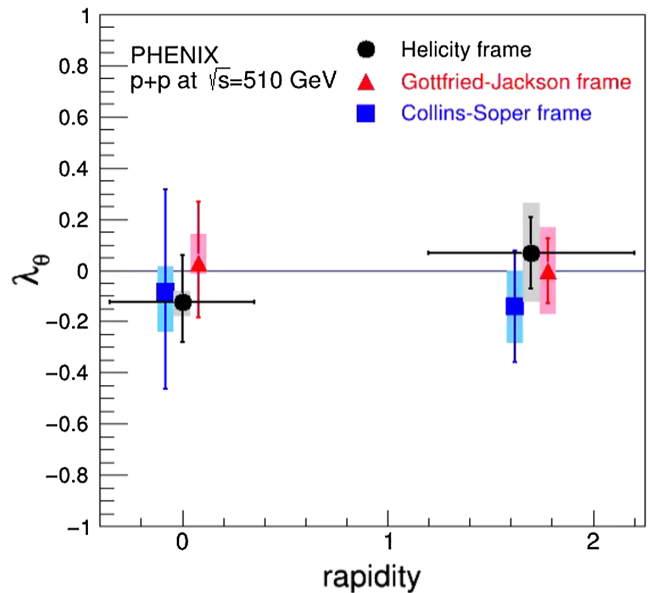

FIG. 14.   Angular coefficient λ_θ of J/ψ production at $\sqrt{s} = 510$ GeV shown as a function of rapidity in three polarization frames. The points for different frames are shifted for clarity. Forward rapidity points are from Ref. [13].

transverse polarization corresponds to the value of 1, and longitudinal polarization corresponds to the value of -1. The zero value seen in $\tilde{\lambda}$ is interpreted as no net polarization. The other variable F also carries similar meaning. Unlike $\tilde{\lambda}$, F is mathematically bounded between 0 and 1. The zero polarization corresponds to $\frac{1}{3}$ and transverse and longitudinal polarization to $\frac{2}{3}$ and 0, respectively.

Two scenarios were considered for these frame-invariant results, NRQCD and the color-singlet model, which is equivalent to the $v \to 0$ limit of NRQCD. The uncertainties on CSM predictions include the scale uncertainty. The CSM prediction is qualitatively opposite to the NRQCD predictions [40,41]. NRQCD predicts transverse polarization, while the CSM predicts longitudinal polarization, as is shown in Figs. 11 and 12. The data do not conclusively exclude either strong transverse or longitudinal polarization.

Results are also compared to previous PHENIX measurements at a different beam energy [12] and rapidity [13]. Figure 13 compares λ_θ in the helicity frame for different collision energies. At midrapidity, the decay lepton spin alignment is consistent with no polarization both at $\sqrt{s} = 200$ (one-dimensional analysis) and 510 GeV (two-dimensional analysis). The rapidity dependence of λ_θ and $\tilde{\lambda}$ is shown in Figs. 14 and 15, respectively. While midrapidity data indicate no polarization, moderate polarization is seen at forward rapidity. At forward rapidity, $\tilde{\lambda}$ was measured to be largely negative, indicating longitudinal polarization. This is in stark contrast to this result that sees no preferred polarization direction, shown in
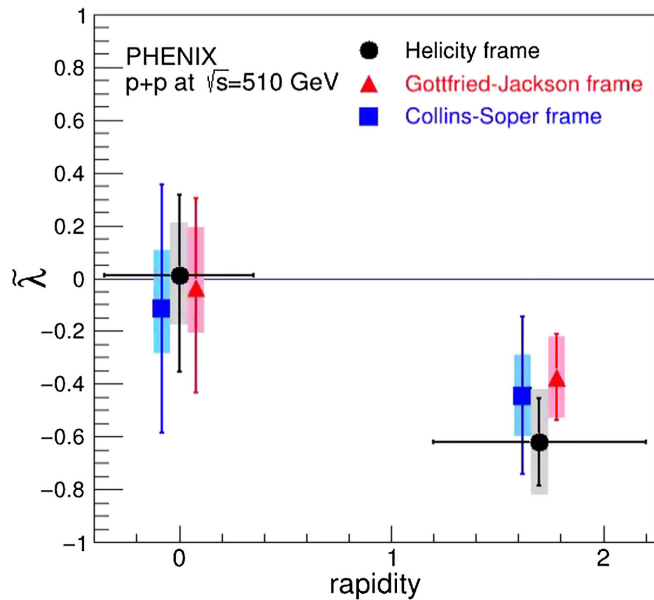
FIG. 15. Rapidity dependence of $\tilde{\lambda}$ of J/ψ production at $\sqrt{s} = 510$ GeV in three polarization frames. The points for different frames are shifted for clarity. Forward rapidity points are from Ref. [13].

Figs. 14 and 15. No strong polarization was seen in other experiments at higher p_T and higher beam energies in general, and the discrepancy between measurements and theory predictions is still being studied. Results of polarization measurements are summarized in Table I.

V. SUMMARY

The PHENIX experiment measured the J/ψ polarization at midrapidity in $\sqrt{s} = 510$ GeV $p + p$ collisions by reconstructing the hadronized charmonium state in the dielectron decay channel. The midrapidity cross section at $\sqrt{s} = 510$ GeV in the same channel has been newly measured and is consistent with NRQCD calculations above $p_T \gtrsim 2$ GeV/c. The results show the expected hardening of the J/ψ p_T spectrum as compared to the measurement at $\sqrt{s} = 200$ GeV. At both low p_T and high p_T, the net polarization has been observed to be consistent with zero within uncertainties. This is in contrast to the measurements made at forward rapidity. The new results do not rule out either the CSM or the NRQCD J/ψ production models. The

new measurements from the two-dimensional analysis show consistency in λ_θ with the results from a previous one-dimensional midrapidity analysis at $\sqrt{s} = 200$ GeV.

[1] N. Brambilla *et al.*, Heavy quarkonium: Progress, puzzles, and opportunities, Eur. Phys. J. C **71**, 1534 (2011).

[2] J.-P. Lansberg, New observables in inclusive production of quarkonia, arXiv:1903.09185.

[3] G. P. Lepage, L. Magnea, C. Nakhleh, U. Magnea, and K. Hornbostel, Improved nonrelativistic QCD for heavy-quark physics, Phys. Rev. D **46**, 4052 (1992).

[4] G. T. Bodwin, E. Braaten, and G. P. Lepage, Rigorous QCD analysis of inclusive annihilation and production of heavy quarkonium, Phys. Rev. D **51,** 1125 (1995); Erratum, Phys. Rev. D **55,** 5853 (1997).

[5] P. Cho and A. K. Leibovich, Color-octet quarkonia production, Phys. Rev. D **53,** 150 (1996).

[6] P. Cho and A. K. Leibovich, Color-octet quarkonia production. II, Phys. Rev. D **53,** 6203 (1996).

[7] Y.-Q. Ma, K. Wang, and K.-T. Chao, Complete next-to-leading order calculation of the J/ψ and ψ production at hadron colliders, Phys. Rev. D **84,** 114001 (2011).

[8] K.-T. Chao, Y.-Q. Ma, H.-S. Shao, K. Wang, and Y.-J. Zhang, J/ψ Polarization at Hadron Colliders in Nonrelativistic QCD, Phys. Rev. Lett. **108,** 242004 (2012).

[9] M. Butenschön and B. A. Kniehl, World data of J/ψ production consolidate nonrelativistic QCD factorization at next-to-leading order, Phys. Rev. D **84,** 051501 (2011).

[10] B. Gong, L.-P. Wan, J.-X. Wang, and H.-F. Zhang, Polarization for Prompt J/ψ and $\psi(2s)$ Production at the Tevatron and LHC, Phys. Rev. Lett. **110,** 042002 (2013).

[11] A. Abulencia et al. (CDF Collaboration), Polarizations of J/ψ and $\psi(2S)$ Mesons Produced in $p\bar{p}$ Collisions at $\sqrt{s} = 1.96$ TeV, Phys. Rev. Lett. **99,** 132001 (2007).

[12] A. Adare et al. (PHENIX Collaboration), Transverse momentum dependence of J/ψ polarization at midrapidity in $p + p$ collisions at $\sqrt{s} = 200$ GeV, Phys. Rev. D **82,** 012001 (2010).

[13] A. Adare et al. (PHENIX Collaboration), Angular decay coefficients of J/ψ mesons at forward rapidity from $p + p$ collisions at $\sqrt{s} = 510$ GeV, Phys. Rev. D **95,** 092003 (2017).

[14] B. Abelev et al. (ALICE Collaboration), J/ψ Polarization in pp Collisions at $\sqrt{s} = 7$ TeV, Phys. Rev. Lett. **108,** 082001 (2012).

[15] S. Chatrchyan et al. (CMS Collaboration), Measurement of the prompt J/ψ and $\psi(2S)$ polarizations in pp collisions at $\sqrt{s} = 7$ TeV, Phys. Lett. B **727,** 381 (2013).

[16] R. Aaij et al. (LHCb Collaboration), Measurement of J/ψ polarization in pp collisions at $\sqrt{s} = 7$ TeV, Eur. Phys. J. C **73,** 2631 (2013).

[17] S. Acharya et al. (ALICE Collaboration), Measurement of the inclusive J/ψ polarization at forward rapidity in pp collisions at $\sqrt{s} = 8$ TeV, Eur. Phys. J. C **78,** 562 (2018).

[18] M. Jacob and G. C. Wick, On the general theory of collisions for particles with spin, Ann. Phys. (N.Y.) **7,** 404 (1959).

[19] J. C. Collins and D. E. Soper, Angular distribution of dileptons in high-energy hadron collisions, Phys. Rev. D **16,** 2219 (1977).

[20] K. Gottfried and J. D. Jackson, On the general theory of collisions for particles with spin, Nuovo Cimento **33,** 309 (1964).

[21] P. Faccioli, C. Loureno, J. Seixas, and H. K. Wöhri, Towards the experimental clarification of quarkonium polarization, Eur. Phys. J. C **69,** 657 (2010).

[22] P. Faccioli, C. Loureno, J. Seixas, and H. K. Wöhri, Model-independent constraints on the shape parameters of dilepton angular distributions, Phys. Rev. D **83,** 056008 (2011).

[23] Y.-Q. Ma, J.-W. Qiu, and H. Zhang, Rotation-invariant observables in polarization measurements, arXiv:1703.04752.

[24] J. C. Martens, J. P. Ralston, and J. D. Tapia Takaki, Quantum tomography for collider physics: Illustrations with lepton-pair production, Eur. Phys. J. C **78,** 5 (2018).

[25] M. Gavrilova and O. Teryaev, Rotation-invariant observables as density matrix invariants, Phys. Rev. D **99,** 076013 (2019).

[26] M. Baumgart, A. K. Leibovich, T. Mehen, and I. Z. Rothstein, Probing quarkonium production mechanisms with jet substructure, J. High Energy Phys. 11 (2014) 003.

[27] Z.-B. Kang, J.-W. Qiu, F. Ringer, H. Xing, and H. Zhang, J/ψ Production and Polarization Within a Jet, Phys. Rev. Lett. **119,** 032001 (2017).

[28] L. Dai and P. Shrivastava, Quarkonium polarization and the long distance matrix elements hierarchies using jet substructure, Phys. Rev. D **96,** 036020 (2017).

[29] R. Bain, L. Dai, A. Leibovich, Y. Makris, and T. Mehen, NRQCD Confronts LHCb Data on Quarkonium Production within Jets, Phys. Rev. Lett. **119,** 032002 (2017).

[30] K. Adcox et al. (PHENIX Collaboration), PHENIX detector overview, Nucl. Instrum. Methods Phys. Res., Sect. A **499,** 469 (2003).

[31] S. S. Adler et al. (PHENIX Collaboration), The relativistic heavy ion collider project: RHIC and its detectors— PHENIX on-line systems, Nucl. Instrum. Methods Phys. Res., Sect. A **499,** 560 (2003).

[32] S. S. Adler et al. (PHENIX Collaboration), J/ψ Production from Proton Proton Collisions at $\sqrt{s} = 200$-GeV, Phys. Rev. Lett. **92,** 051802 (2004).

[33] M. Oreglia, A study of the reactions $\psi' \to \gamma\gamma\psi$, Ph.D. thesis, SLAC-R-236, 1980.

[34] T. Hastie, R. Tibshirani, and J. Friedman, The Elements of Statistical Learning, Springer Series in Statistics (Springer, New York, New York, 2001).

[35] M. Butenschön and B. A. Kniehl, Reconciling J/ψ Production at HERA, RHIC, Tevatron, and LHC with Nonrelativistic QCD Factorization at Next-to-Leading Order, Phys. Rev. Lett. **106,** 022003 (2011).

[36] A. Adare et al. (PHENIX Collaboration), J/ψ Production Versus Transverse Momentum and Rapidity in p^+p Collisions at $\sqrt{s} = 200$-GeV, Phys. Rev. Lett. **98,** 232002 (2007).

[37] K. Aamodt et al. (ALICE Collaboration), Rapidity and transverse momentum dependence of inclusive J/ψ production in pp collisions at $\sqrt{s} = 7$ TeV, Phys. Lett. B **704,** 442 (2011); Erratum, Phys. Lett. B **718,** 692 (2012).

[38] B. Abelev et al. (ALICE Collaboration), Inclusive J/ψ production in pp collisions at $\sqrt{s} = 2.76$ TeV, Phys. Lett. B **718,** 295 (2012); Erratum, Phys. Lett. B **748,** 472 (2015).

[39] D. Acosta et al. (CDF Collaboration), Measurement of the J/ψ meson and b–hadron production cross sections in $p\bar{p}$ collisions at $\sqrt{s} = 1960$ GeV, Phys. Rev. D **71,** 032001 (2005).

[40] M. Butenschön and B. A. Kniehl, J/ψ Polarization at the Tevatron and the LHC: Nonrelativistic-QCD Factorization at the Crossroads, Phys. Rev. Lett. **108,** 172002 (2012).

[41] M. Butenschön and B. A. Kniehl, Next-to-leading order tests of nonrelativistic-QCD factorization with J/ψ yield and polarization, Mod. Phys. Lett. A **28,** 1350027 (2013).

Correction: An outdated manuscript was used instead of a revised version during preparation for publication. The correct file has been processed, with a new Ref. [24] cited in Sec. I.